Pergamon

Acta mater. Vol. 46, No. 6, pp. 2113–2130, 1998

Printed in Great Britain
PII: S1359-6454(97)00377-7
1359-6454/98 $19.00 + 0.00

A DIFFUSE INTERFACE MODEL FOR MICROSTRUCTURAL EVOLUTION IN ELASTICALLY STRESSED SOLIDS

P. H. LEO[1], J. S. LOWENGRUB[2] and H. J. JOU[3]

[1]Department of Aerospace Engineering and Mechanics, University of Minnesota, Minneapolis, MN 55455, U.S.A., [2]School of Mathematics, University of Minnesota, Minneapolis, MN 55455, U.S.A. and [3]Department of Engineering, Colorado School of Mines, Golden, CO 80401, U.S.A.

(*Received 14 August 1997; accepted 10 October 1997*)

Abstract—We present a diffuse interface (DI) model for capturing microstructure formed during the coarsening of a two dimensional, elastically stressed binary alloy. The DI model is based on a generalized Cahn–Hilliard free energy; evolution occurs to lower the free energy. Using a matched asymptotic expansion, we show that the DI model converges to a well-studied sharp interface system as the thickness of the diffuse interface approaches zero. Numerical simulations confirm this equivalence. We develop pseudo-spectral numerical methods to solve the DI system and we carefully investigate the dependence of results on numerical parameters. The DI model is used to follow microstructural evolution through topological transitions such as particle merging and vanishing. We show that in isotropic media, elastic inhomogeneity may lead to interesting topology changes such as a reversal of the roles of the precipitate and matrix phases. © *1998 Acta Metallurgica Inc.*

1. INTRODUCTION

In this paper, we present a diffuse interface model for capturing microstructures formed during the coarsening of a two dimensional, elastically stressed binary alloy. The interest in such systems stems from observations (primarily in nickel superalloys) that microstructures depend nontrivially on both the elastic and diffusion fields in the system [1–5]. These observations include transitions from spherical to cuboidal to plate-shaped precipitates, precipitate alignment, precipitate merging and splitting and dendritic shapes during growth. Unlike surface energy, elastic energy does not necessarily favor large precipitates over smaller ones. Consequently, it may be possible to use elastic fields to control and stabilize the coarsening process.

The model we adopt is based on a generalized free energy functional of Cahn–Hilliard type [6–8]. Interfaces are diffuse, i.e. they consist of smooth, but rapid transitions of both the concentration and elastic displacement fields. The microstructural evolution is modelled by a set of partial differential equations such that the generalized free energy is nonincreasing in time.

In an alternative approach, the precipitate–matrix interfaces can be taken to be $(n-1)$-dimensional surfaces ($n = 2$ or 3). In this case, the microstructural evolution is described by field equations in the bulk phases with jump conditions at the interfaces.

An advantage of the sharp interface approach is that the system can be reformulated as boundary integral equations for which very efficient numerical methods have been developed. This approach has been used to study microstructural features such as particle translation, equilibrium shapes, shape bifurcations and particle growth (e.g. [9–18]). A disadvantage of sharp interface methods is that mathematical singularities form when particles vanish, merge or split; such transitions can be bridged only with *ad hoc* methods. In contrast, diffuse interface (DI) methods naturally handle topological changes. These methods have been previously used to study the effect of elastic fields on spinodal decomposition, precipitate shapes and motions, and shape transitions such as particle splitting and merging (e.g. [19–24]).

Our goals in this work are: (1) to connect, both analytically and numerically, the diffuse and sharp interface approaches, (2) to develop and analyze robust numerical algorithms to solve the system of equations associated with the DI method and (3) to explore the role of elastic inhomogeneities on microstructural evolution and, in particular, topological transitions.

We achieve these goals as follows. First, we show that in the limit as the interfacial thickness vanishes, the DI system converges to the sharp interface model presented in [12] with diffusion in both the precipitate and matrix phases. We present numerical simulations which confirm this agreement. Second, we develop numerical algorithms to solve the DI system and we investigate their accuracy. We show that certain details of the solution, such as the chemical potential, are sensitive to the numerical al-

gorithms. However, macroscopic quantities such as particle shapes and merging behavior, are essentially unaffected by the algorithms.

Third, we consider two types of elastic media: anisotropic, homogeneous and isotropic, inhomogeneous. These choices are motivated by the existence of efficient boundary integral methods for these two cases. In the DI approach, the elastic inhomogeneity is modelled by taking a stiffness tensor that varies smoothly with composition. Consistent with the results of [12], we find that inhomogeneity plays an important role in microstructural evolution. For example, in anisotropic, homogeneous elastic media, there is a stable interparticle spacing. However, in inhomogeneous, isotropic media, we find that precipitates with dilatational misfit and a lower shear modulus than the matrix tend to merge while those with shear modulus higher than the matrix tend to repel. We find some interesting topology changes that lead to a reversal of the roles of the precipitate and matrix phases.

The paper is organized as follows. In Sections 2 and 3, we give the governing equations for the sharp and DI models. In Section 4, we present results from an asymptotic analysis to show the equivalence of the two approaches in a certain limit. In Section 5, we discuss the numerical implementation of the DI model. In Section 6, we compare the results from the two methods and we present some new numerical results involving topological transitions using the DI model. Finally, in Section 7 we give our conclusions.

2. SHARP INTERFACE MODEL

In this Section, we briefly discuss the multi-phase diffusion problem under the assumption that the interfaces between the precipitate and matrix phases are sharp (zero thickness). A more detailed discussion can be found in [12].

The matrix and precipitate phases occupy the two dimensional plane $\mathbf{R}^2$. The matrix phase Ω^{M} is assumed to be infinite in extent, while the precipitate phase Ω^{P} consists of p separate particles occupying a finite area. We define Γ to be the collection of all the individual interfaces.

We assume that diffusion occurs in the matrix only (one-sided diffusion) and is quasistatic. Thus the composition c of the diffusing species obeys Laplace's equation in Ω^{M}. We take zero flux of mass into the system and we suppose that the nondimensional normal velocity V on an interface is given by $V = \nabla c \cdot \mathbf{n}$ on that interface, where $\mathbf{n}$ is the outward unit normal; this is appropriate for the one-sided diffusion problem.

The boundary condition for the matrix composition on Γ is given by a generalized Gibbs-Thomson equation valid for coherent interfaces,

$$c = \kappa + ZG^{\mathrm{el}} \tag{1}$$

Here, κ is the dimensionless mean curvature and

$$G^{\mathrm{el}} = \frac{1}{2}\mathcal{S}^{\mathrm{P}}_{ij}(\mathcal{E}^{\mathrm{P}}_{ij} - \mathcal{E}^{\mathrm{T}}_{ij}) - \frac{1}{2}\mathcal{S}^{\mathrm{M}}_{ij}\mathcal{E}^{\mathrm{M}}_{ij} + \mathcal{S}^{\mathrm{M}}_{ij}(\mathcal{E}^{\mathrm{M}}_{ij} - \mathcal{E}^{\mathrm{P}}_{ij}), \tag{2}$$

is a dimensionless elastic energy density, see [25]. In G^{el}, $\mathcal{E}^{\chi}_{ij}$ is the usual infinitesimal strain tensor, where $\chi = \mathrm{M}$ or P for matrix or precipitate, S^{χ} denotes the stress tensors (defined below) and Z is a nondimensional parameter that characterizes the relative contribution of the elastic and surface energies.

The presence of G^{el} in the boundary condition (equation (1)) requires one to solve the two phase elasticity problem in addition to the diffusion problem. Following Eshelby [25, 26], we take the reference state to be the unstressed lattice of the matrix, so that

$$\mathcal{S}^{\mathrm{M}}_{ij} = \mathcal{C}^{\mathrm{M}}_{ijkl}\mathcal{E}^{\mathrm{M}}_{kl} \tag{3}$$

in the matrix, and

$$\mathcal{S}^{\mathrm{P}}_{ij} = \mathcal{C}^{\mathrm{P}}_{ijkl}(\mathcal{E}^{\mathrm{P}}_{kl} - \mathcal{E}^{\mathrm{T}}_{kl}), \tag{4}$$

in the precipitate. In equation (4), $\mathcal{E}^{\mathrm{T}}_{kl}$ is the misfit (transformation) strain, which maps the unstressed precipitate lattice to that of the matrix. Also, $\mathcal{C}^{\chi}_{ijkl}$ denotes the stiffness tensor of the $\chi = \mathrm{P}$, M phase, which is taken to be constant.

As mentioned in the introduction, we consider both the elastically isotropic, inhomogeneous case and the elastically anisotropic, homogeneous case. In the former, we normalize the shear modulus in the matrix $G^{\mathrm{M}} = 1$ so that the stiffness tensor is

$$\mathcal{C}^{\chi}_{ijkl} = 2G^{\chi}\delta_{ik}\delta_{jl} + \frac{2G^{\chi}\nu^{\chi}}{1 - 2\nu^{\chi}}\delta_{ij}\delta_{kl}, \tag{5}$$

where G^{P} is the (normalized) shear modulus of the precipitate and ν^{M} and ν^{P} are appropriate Poisson ratios. We note that in this case we take,

$$Z = \tilde{G}^{\mathrm{M}}(\mathcal{E}^{\mathrm{T}}_{11})^2\tilde{L}/\tilde{\tau}, \tag{6}$$

where $\tilde{G}^{\mathrm{M}}$ and $\tilde{\tau}$ are the *dimensional* values of the matrix shear modulus and surface energy, respectively, $\tilde{L}$ is a length scale (usually taken to be an average initial precipitate radius) and $\mathcal{E}^{\mathrm{T}}_{11}$ is the value of the 1–1 component of the misfit strain.

In the anisotropic, homogeneous case, we normalize the cubic elastic constant $C_{44} = 1$ and we write the stiffness tensor $\mathcal{C} = \mathcal{C}^{\mathrm{M}} = \mathcal{C}^{\mathrm{P}}$ as

$$\mathcal{C}_{ijkl} = 2\delta_{ik}\delta_{jl} + C_{12}\delta_{ij}\delta_{kl} + (C_{11} - C_{12} - 2)\delta_{ijkl} \tag{7}$$

in terms of the remaining constants C_{11} and C_{12}. In this case,

$$Z = \tilde{C}_{44}(\mathcal{E}^{\mathrm{T}}_{11})^2\tilde{L}/\tilde{\tau} \tag{8}$$

where $\tilde{C}_{44}$ is the *dimensional* value of the elastic constant.

To complete the formulation of the elasticity problem, we require that the divergence of stress tensor vanishes in both the precipitate and matrix

domains. We also specify that the precipitate–matrix interfaces are coherent, i.e. there is continuity of displacement and traction across Γ. We assume that the stresses and strains in the matrix vanish in the far-field (i.e. no applied load). Finally, we note that the multiphase system can be characterized by a nonincreasing energy function $E(t)$, which is the sum of the surface and strain energies.

The reformulation of the above problem in terms of boundary integral equations, and their subsequent numerical solution, is discussed extensively in [12]. We refer the interested reader there for details.

3. DIFFUSE INTERFACE MODEL

In this Section, we present the diffuse interface model. The model we consider is motivated by the approach of Cahn and Hilliard [6] and Cahn [7] on spinodal decomposition in alloys. A derivation of the model, using "microforce" balances, is given by Gurtin [8].

In the model, the sharp interface is replaced by a narrow transition layer across which all quantities are assumed to vary smoothly. For example, the composition c varies smoothly across the layer from $c = c_M$, the composition of the "pure" matrix phase, to $c = c_P$, the composition of the "pure" precipitate phase. The stiffness and misfit tensors are interpolated across the precipitate–matrix boundaries by

$$\mathcal{C}(c) = \mathcal{C}^M + g(c)(\mathcal{C}^P - \mathcal{C}^M) \text{ and } \mathcal{E}^T(c) = h(c)\mathcal{E}^T. \quad (9)$$

Here, $\mathcal{C}^P$ and $\mathcal{C}^M$ are the constant stiffness tensors in the precipitate and matrix phases, $\mathcal{E}^T$ is the constant misfit tensor, and $g(c)$ and $h(c)$ are scalar interpolation functions such that $g(c_M) = h(c_M) = 0$ and $g(c_P) = h(c_P) = 1$.

In the model, evolution is specified such that a certain generalized free energy functional decreases. This free energy functional is analogous to the energy in the sharp interface model and is the sum of a generalized elastic energy and a generalized surface energy. The generalized free energy is given in terms of a specific free energy Ψ by

$$E(t) = \int_\Omega \Psi(\mathcal{E},\ c,\ \nabla c) \quad \mathrm{d}A, \quad (10)$$

where $\Omega = \Omega^P \bigcup \Omega^M$ and we do not explicitly distinguish between the precipitate and matrix domains. The specific free energy Ψ is given by

$$\Psi(\mathcal{E},\ c,\ \nabla c) = W(\mathcal{E},\ c) + f(c) + \frac{\gamma^2}{2}|\nabla c|^2. \quad (11)$$

The first term

$$W(\mathcal{E},\ c) = \gamma\frac{Z}{2}(\mathcal{E} - \mathcal{E}^T(c)) : \mathcal{C}(c)(\mathcal{E} - \mathcal{E}^T(c)), \quad (12)$$

is the strain energy, where the tensor product: is defined by $\mathcal{E}:\mathcal{F} = \mathcal{E}_{ij}\mathcal{F}_{ij}$. The presence of the coefficient γ in $W(\mathcal{E}, c)$ is necessary in order for the diffuse interface system to converge to the sharp interface system, described in Section 2, in the limit as $\gamma \to 0$. See Section 4.

The second and third terms in Ψ together form the generalized surface energy. The second term $f(c)$ is the bulk chemical energy and, as in the classic Cahn–Hilliard work, is taken to be a double-welled potential so that the system separates into a phase (precipitate phase) with composition c_P and a (matrix) phase with composition c_M. For simplicity, in this paper, we will take

$$f(c) = \frac{A^2}{4}c^2(1-c)^2, \quad (13)$$

where A is a parameter that will be used to tune the numerical value of the surface tension (see Section 4). We also set $c_P = 1$ and $c_M = 0$. The third term in Ψ, $\gamma^2|\nabla c|^2/2$, is a gradient energy that acts to stabilize the interfacial transition region. This gradient energy, together with $f(c)$, keeps the thickness of the region proportional to γ.

Now, the evolution of the diffusion and elasticity fields in this formulation are given by

$$\dot{c} = \nabla \cdot \left(\frac{1}{\gamma}\nabla\mu\right), \quad (14)$$

$$\nabla \cdot \mathcal{S} = 0, \quad (15)$$

where $1/\gamma$ is a mobility,

$$\mu = \frac{\delta\Psi}{\delta c} = \frac{\partial\Psi}{\partial c}(\mathcal{E},\ c,\ \nabla c) - \nabla \cdot \left(\frac{\partial\Psi}{\partial\nabla c}\right) \quad (16)$$

is a generalized chemical potential [8] and

$$\mathcal{S} = \frac{\partial\Psi}{\partial\mathcal{E}}(\mathcal{E},\ c,\ \nabla c) \quad (17)$$

is the generalized stress tensor. Taking γ small scales the diffusional kinetics to a long time limit, and allows us to recapture quasistatic diffusion as $\gamma \to 0$ (again see Section 4). A straightforward calculation yields the following explicit form for the chemical potential

$$\mu = f'(c) - \gamma^2\Delta c - \gamma Z\mathcal{E}^{T\prime}(c) : \mathcal{C}(c)(\mathcal{E} - \mathcal{E}^T(c)) + \gamma\frac{Z}{2}(\mathcal{E} - \mathcal{E}^T(c)) : \mathcal{C}'(c)(\mathcal{E} - \mathcal{E}^T(c)), \quad (18)$$

where $\mathcal{C}'(c) = g'(c)(\mathcal{C}^P - \mathcal{C}^M)$ and $\mathcal{E}^{T\prime}(c) = h'(c)\mathcal{E}^T$ and the stress

$$\mathcal{S} = \gamma Z\mathcal{C}(c)(\mathcal{E} - \mathcal{E}^T(c)). \quad (19)$$

The "elasticity" equation (15) may also be written in terms of the displacement vector $\mathbf{u}$ as

$$\frac{1}{2}\nabla \cdot [\mathcal{C}(c)(\nabla\mathbf{u} + \nabla\mathbf{u}^T)] = \nabla \cdot [\mathcal{C}(c)\mathcal{E}^T(c)], \quad (20)$$

using equations (15) and (19) and the definition of the infinitesimal strain.

For the system of equations (14) and (15), the generalized free energy of equation (10) is non-increasing and satisfies

$$\dot{E} = -\frac{1}{\gamma}\int_{\Omega} |\nabla \mu|^2 \mathrm{d}A. \tag{21}$$

for periodic or natural boundary conditions.

We note that similar approaches for solid–solid phase transformations have been well-established in the literature (e.g. see Fried and Gurtin [27], Fried and Grach [28], Wang and Khachaturyan [22] and Voorhees *et al.* [29]). The diffuse interface model of equations (14) and (15) naturally fits into general framework of phase-field models which have been widely used in the study of free boundary problems (see [30] for a collection of recent references).

4. MATHEMATICAL COMPARISON OF THE MODELS

In this Section, we demonstrate the sense in which sharp and diffuse interface approaches are mathematically equivalent. In the diffuse interface model, the parameter γ is a measure of the thickness of the interfacial regions. Therefore, we consider the sharp interface limit of the diffuse equations ($\gamma \to 0$) and under the appropriate restrictions, we show that the limiting system is equivalent to the sharp interface model described in Section 2. We follow the approach of Pego [31] and use the method of matched asymptotic expansions to analyze the limiting process (see also [32, 33] for further references). Here, we only present the result of this procedure. The details of the matched asymptotic expansion are sketched very briefly in Appendix A; see also [34].

Suppose that there is a narrow transition layer separating the matrix and precipitate phases. If there are several transition layers, we suppose they are well-separated. The transition layer separates the plane Ω into Ω^{P} and Ω^{M}, where the composition of solute is nearly equal to 1 in Ω^{P} and 0 in Ω^{M}. We further suppose that the transition layer contains a smooth, closed interface Γ. Let c, $\mathcal{S}$ be the composition and stress solutions of the diffuse interface equations (14) and (15) in the presence of a transition layer. In addition, let $c_{\mathrm{M}} = 0$ and $c_{\mathrm{P}} = 1$ and define the scaled composition field

$$\tilde{c} = f''(c_\chi)(c - c_\chi)/\gamma, \text{ in } \Omega^\chi, \tag{22}$$

with $\chi = \mathrm{M}$ or P. Then, for γ small, $\tilde{c}$ and $\mathcal{S}$ satisfy

$$\Delta\tilde{c} = -\Delta\frac{\partial \tilde{W}}{\partial c}(\mathcal{E}, c_\chi) + O(\gamma), \text{ and } \nabla \cdot \mathcal{S} = 0, \tag{23}$$

in Ω^χ where

$$\mathcal{S} = \mathcal{C}^{\mathrm{M}}\mathcal{E} + O(\gamma) \text{ in } \Omega^{\mathrm{M}}, \text{ and}$$

$$\mathcal{S} = \mathcal{C}^{\mathrm{P}}(\mathcal{E} - \mathcal{E}^{\mathrm{T}}) + O(\gamma) \text{ in } \Omega^{\mathrm{P}} \tag{24}$$

are the stress tensors in each domain. Further, by $O(\gamma^p)$, we denote all the higher order terms that behave like γ^p as $\gamma \to 0$. Finally, the leading order source term in the concentration equation (23) is given by

$$\frac{\partial \tilde{W}}{\partial c}(\mathcal{E}, c_\chi) = Z[h'(c_\chi)\mathcal{E}^{\mathrm{T}} : \mathcal{C}(c_\chi)(\mathcal{E} - \mathcal{E}^{\mathrm{T}}(c_\chi))$$

$$+ \frac{1}{2}g'(c_\chi)(\mathcal{E} - \mathcal{E}^{\mathrm{T}}(c_\chi)) : (\mathcal{C}^{\mathrm{P}} - \mathcal{C}^{\mathrm{M}})(\mathcal{E} - \mathcal{E}^{\mathrm{T}}(c_\chi))]. \tag{25}$$

Consequently, to leading (zeroth) order, the stress satisfies the usual elasticity equations while the scaled composition field $\tilde{c}$ satisfies a two-sided Poisson equation where the source term depends on the elastic fields. Note that in the sharp interface case we considered in Section 2, there was no such source term as the concentration field satisfied Laplace's equation in the matrix domain Ω^{M}. To eliminate the source term in the leading order concentration equation and hence to have $\tilde{c}$ satisfy Laplace's equation (in both domains Ω^{P} and Ω^{M}), we set

$$g'(c_{\mathrm{M}}) = g'(c_{\mathrm{P}}) = h'(c_{\mathrm{M}}) = h'(c_{\mathrm{P}}) = 0. \tag{26}$$

These conditions guarantee that the interpolation is very smooth in the regions of near homogeneity. In this paper, we take $g(c) = h(c) = 3c^2 - 2c^3$.

The boundary conditions are as follows. On Γ, we find that to leading order, the coherent boundary conditions are satisfied, i.e.

$$\mathbf{u}|_{\mathrm{M}} = \mathbf{u}|_{\mathrm{P}} + O(\gamma), \text{ and } \mathbf{t}_{\mathrm{M}} = \mathbf{t}|_{\mathrm{P}} + O(\gamma), \tag{27}$$

where $|_\chi$ denotes the limit onto Γ from the domain Ω^χ and $\mathbf{t} = S\mathbf{n}$ is the traction vector. For the scaled composition field, we find that

$$\tilde{c}|_{\mathrm{M}} = \tilde{c}|_{\mathrm{P}} = \tau\kappa + ZG^{\mathrm{el}} + O(\gamma), \tag{28}$$

where the surface tension τ is given by

$$\tau = \int_0^1 \sqrt{2f(c)}\,\mathrm{d}c = A/(6\sqrt{2}), \tag{29}$$

where we have used equation (13). Thus, if we set $A = 6\sqrt{2}$ (so that $\tau = 1$), then to leading order, equation (28) reduces to the generalized Gibbs–Thomson boundary condition of equation (1).

Finally, the normal velocity V of Γ is given by

$$V = (\nabla\tilde{c}|_{\mathrm{M}} - \nabla\tilde{c}|_{\mathrm{P}}) \cdot \mathbf{n} + O(\gamma), \tag{30}$$

which is the flux balance appropriate for two-sided diffusion.

In summary, we find that the leading order equations and boundary conditions satisfied by the diffuse interface solutions are *exactly* those used in the sharp interface description except that in the diffuse case, the quasi-static diffusion is two-sided. To obtain one-sided diffusion from the smooth interface approach, the mobility $1/\gamma$ in equation (14) would have to be replaced by a function (scaled by $1/\gamma$) which vanishes in the precipitate region. In

addition, the far-field boundary conditions for both the composition and elasticity fields in the diffuse interface approach can be chosen to match those from the sharp interface approach.

5. NUMERICAL IMPLEMENTATION OF DIFFUSE INTERFACE MODEL

In this Section, we present the numerical implementation of equations (14) and (15) for the diffuse interface model. Unlike the boundary integral approach, we impose periodic boundary conditions in both x and y and we use a pseudo-spectral method in space (derivatives are obtained using the fast Fourier transform (FFT) and products are performed in physical space) together with a non-stiff updating scheme in time for the evolution of the composition field.

The sequence of the scheme is: (1) solve the elasticity equations in displacement form and evaluate the generalized chemical potential μ, (2) update the composition field and (3) repeat. We now discuss each step separately.

5.1. Solution of elasticity equations

We consider two cases: (i) cubic anisotropic, homogeneous elasticity and (ii) isotropic, inhomogeneous elasticity. In each case, we solve the elasticity equations in displacement form. From the displacements, we then obtain the stresses and strains. We begin with a discussion of case (i).

For *cubic anisotropic, homogeneous* elasticity, the displacement equation (equation (20)), in component form, reduces to

$$C_{11}u_{1,11} + (C_{12} + C_{44})u_{2,12} + u_{1,22} = h'(c)T_{1j}c_{,j} \quad (31)$$

$$C_{11}u_{2,22} + (C_{12} + C_{44})u_{1,12} + u_{2,11} = h'(c)T_{2j}c_{,j} \quad (32)$$

where

$$T_{11} = C_{11}\mathcal{E}^{\mathrm{T}}_{11} + C_{12}\mathcal{E}^{\mathrm{T}}_{22}, \quad T_{22} = C_{11}\mathcal{E}^{\mathrm{T}}_{22} + C_{12}\mathcal{E}^{\mathrm{T}}_{11}, \quad \text{and } T_{12} = 2\mathcal{E}^{\mathrm{T}}_{12}. \quad (33)$$

Recall that we have normalized the elastic coefficients so that $C_{44} = 1$. Because the coefficients of the displacements in equations (31) and (32) are constant, the Fourier transform can be used to solve this system. Using a hat to denote the Fourier transform, we find that the Fourier transforms of the displacement vector can be found explicitly as

$$\begin{pmatrix} \hat{u}_1 \\ \hat{u}_2 \end{pmatrix} = \frac{1}{\alpha\delta - \beta^2} \begin{pmatrix} \delta & -\beta \\ -\beta & \alpha \end{pmatrix} \begin{pmatrix} \hat{r}_1\ (k_1,\ k_2) \\ \hat{r}_2\ (k_1,\ k_2) \end{pmatrix}, \quad (34)$$

where k_1 and k_2 are the Fourier wavenumbers in the x and y directions, respectively, and $\alpha = -(k_1^2 C_{11} + k_2^2 C_{44})$, $\beta = -k_1 k_2 (C_{12} + C_{44})$, $\delta = -(k_2^2 C_{11} + k_1^2 C_{44})$, $r_1 = h'(c)T_{1j}c_{,j}$ and $r_2 = h'(c)T_{2j}c_{,j}$.

Given c, then the displacements u_1 and u_2 are solved in this way using the fast Fourier transform.

For the case of *inhomogeneous, isotropic* elasticity, the displacement equation (20) take the form

$$G(c)u_{i,jj} + (G(c) + \lambda(c))u_{j,ji} + G'(c)(u_{i,j} + u_{j,i})c_{,j} + \lambda'(c)u_{j,j}c_{,i} = 2\mathcal{E}^{\mathrm{T}}_{ij}(G(c)h(c))_{,j} + \mathcal{E}^{\mathrm{T}}_{jj}(\lambda(c)h(c))_{,i}, \quad (35)$$

where

$$G(c) = G^{\mathrm{M}} + g(c)(G^{\mathrm{P}} - G^{\mathrm{M}}), \quad \lambda(c) = \lambda^{\mathrm{M}} + g(c)(\lambda^{\mathrm{P}} - \lambda^{\mathrm{M}}) \quad (36)$$

and $\lambda^{\gamma} = 2G^{\gamma}\nu^{\gamma}/(1 - 2\nu^{\gamma})$ is the Lame constant in the region in the "pure" precipitate or matrix region. Unlike the homogeneous case, this system cannot be solved explicitly using the Fourier transform, because the coefficients of the displacements are variable. However, given c, the operator on the displacement $\mathbf{u}$ is linear, positive definite and symmetric. Therefore, the solution to equation (35) can be found iteratively using the preconditioned conjugate gradient method. The idea behind the preconditioning is as follows. Let $\mathcal{L}$ be the operator on $\mathbf{u}$ in equation (35). Let the preconditioning operator L be given by $L[\mathbf{u}]_i = \bar{G}u_{i,jj} + (\bar{G} + \bar{\lambda})u_{j,ji}$ where $\bar{G}$ and $\bar{\lambda}$ are the spatial averages of G and λ, respectively. Then equation (35) can be rewritten as

$$\mathcal{L}[\mathbf{u}] = (L + \mathcal{R})[\mathbf{u}] = \mathbf{r}.$$

where $\mathcal{R} = \mathcal{L} - L$ and $\mathbf{r}$ denotes the right hand side of equation (35). Because the operator L has constant coefficients, it can be inverted using the FFT by a formula analogous to that in equation (34). Inverting L in this way yields the preconditioned system

$$(I + L^{-1}\mathcal{R})[\mathbf{u}] = L^{-1}\mathbf{r},$$

which is easily solved using the conjugate gradient method. We find this method to be very efficient, usually requiring fewer than three iterations per time step to obtain a residual error of 10^{-8}.

Once the composition c and displacement $\mathbf{u}$ are obtained, the generalized chemical potential μ is computed using equation (18).

5.2. Non-stiff time stepping for composition update

We explicitly separate the highest derivative term (4th derivatives) from the remaining terms in the composition equation (14) as

$$\dot{c} = -\gamma\Delta^2 c + \frac{1}{\gamma}\Delta\mathcal{N}(c, t), \text{ where } \mathcal{N}(c, t) = \mu + \gamma^2\Delta^2 c \quad (37)$$

denotes the remaining nonlinear terms. Since the 4th derivative term is linear in c and has a constant coefficient, it is diagonalized by the Fourier transform. We can therefore take the Fourier transform of equation (37) and use an integrating factor to integrate the 4th derivative term exactly. If we use

the Adams–Bashforth 2nd order method [35] to integrate the nonlinear term $\mathcal{N}(c, t)$, the resulting scheme is given by

$$\hat{c}^{n+1} = e^{-\gamma|k|^4\Delta t}\left[\hat{c}^n - \frac{\Delta t\,|k|^2}{2\gamma}(3\hat{\mathcal{N}}^n - e^{-\gamma|k|^4\Delta t}\hat{\mathcal{N}}^{n-1})\right], \tag{38}$$

where $|k|^2 = k_1^2 + k_2^2$. This scheme, referred to as algorithm A, is designed to be globally stable with respect to the spatial grid spacing. However, we find that in practice, small time steps ($O(10^{-5})$ using $\gamma = 0.15$) are still required for stability. For comparison, we also implemented an implicit time stepping scheme based on the Crank–Nicholson method as well as an explicit time stepping scheme using Euler's method. We found that both these methods were impractical; the Crank–Nicholson method required time steps on the order of $O(10^{-9})$ to be stable while the Euler method required $O(10^{-10})$ time steps for stability.

Although algorithm A is robust, it can lead to equilibria that depend sensitively on the small scales present in the solutions. In algorithm A, the Fourier modes of the solution are damped by the factor $e^{-\gamma|k|^4\Delta t}$ at every time step. Thus, roughly speaking, there is a wavenumber $k_* = k_*(\Delta t)$ such that the modes $|k| > k_*$ are cut-off. This can lead to a time-step dependent smoothing of the high gradients associated with interfacial layers.

This phenomena can be quantified by examining the equilibria associated with differential equation (equation (37)) and the discrete algorithm A in Fourier space. Setting $\dot{c} = 0$ in equation (37), we find that

$$-\gamma^2|k|^2\hat{c} = \hat{\mathcal{N}} + \text{constant}. \tag{39}$$

We note for future reference that this constant depends linearly upon the parameter γ. The corresponding equilibrium of the discrete system of equation (38) can be found by setting $\hat{c}^{n+1} = \hat{c}^n = \hat{c}^*$ and $\hat{\mathcal{N}}^n = \hat{\mathcal{N}}^{n-1} = \hat{\mathcal{N}}^*$, this yields

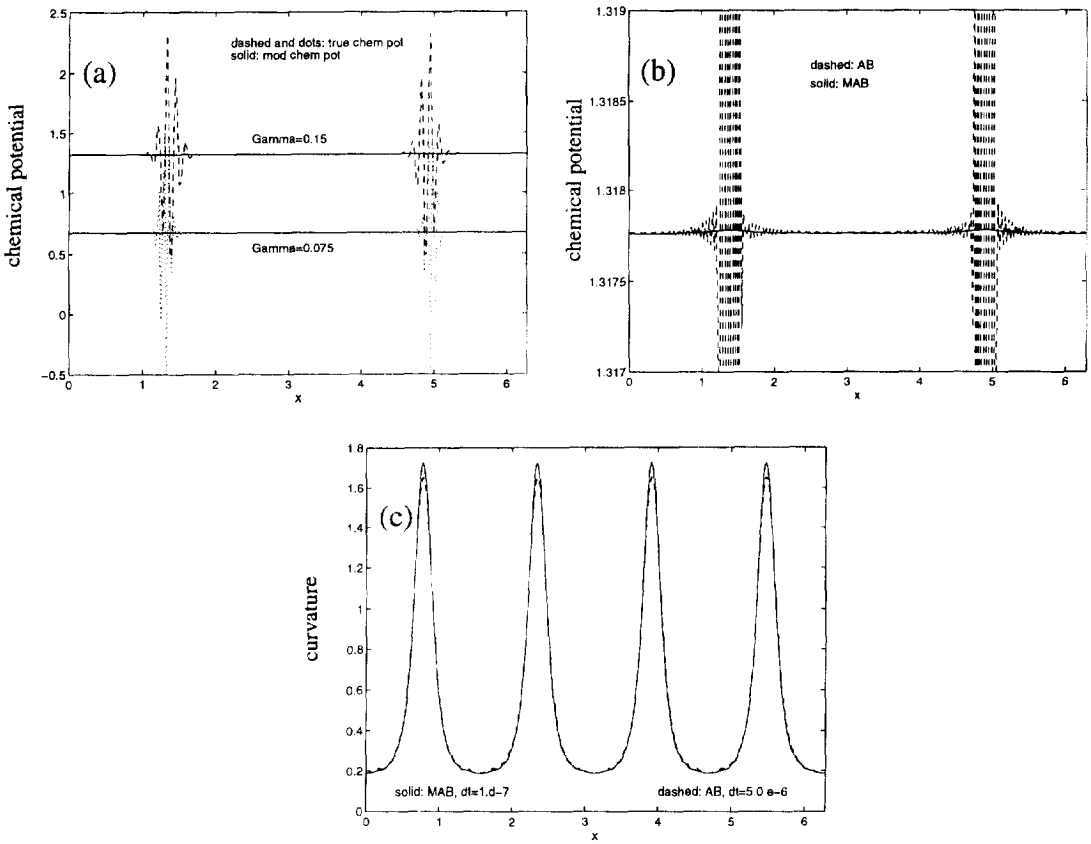

Fig. 1. Chemical Potentials and Curvature. (a) True and modified chemical potentials for algorithm A ($\Delta t = 3 \times 10^{-6}$ for $\gamma = 0.15$, $\Delta t = 7.5 \times 10^{-7}$ for $\gamma = 0.075$); (b) true chemical potentials for algorithm A (AB) and algorithm B (MAB) ($\gamma = 0.15$, $\Delta t = 1 \times 10^{-7}$); (c) curvature of 0.5 composition contour for algorithms A and B (algorithm A: $\Delta t = 5.0 \times 10^{-6}$, algorithm B: $\Delta t = 1 \times 10^{-7}$). In (a)–(c), the spatial grid spacing is $h_1 = h_2 = 2\pi/256$. The elasticity is cubic, anisotropic with $C_{11} = 1.98$, $C_{12} = 1.18$ and $Z = 8$. The misfit is dilatational.

$$\frac{\gamma}{|k|^2\Delta t}(1-e^{-\gamma|k|^4\Delta t})\hat{c}^* = \frac{1}{2}(3e^{-\gamma|k|^4\Delta t} - e^{-2\gamma|k|^4\Delta t})\hat{\mathcal{N}}^* + \text{constant}. \quad (40)$$

A Taylor expansion shows that equations (39) and (40) agree to second order in Δt in the limit $|k|^4\Delta t \to 0$. In practice, however, we find that $|k_*|^4\Delta t$ may not be small which leads to a discrepancy between the formulae at high wavenumbers.

This discrepancy can be made apparent by comparing the true chemical potential μ given in equation (37) with a modified chemical potential

$$\hat{\mu}^* = \frac{1}{2}(3e^{-\gamma|k|^4\Delta t} - e^{-2\gamma|k|^4\Delta t})\hat{\mathcal{N}}^* - \frac{\gamma}{|k|^2\Delta t}(e^{-\gamma|k|^4\Delta t} - 1)\hat{c}^*, \quad (41)$$

which is motivated by equation (40). In Fig. 1(a), the true and modified chemical potentials are shown at a time near the numerical equilibrium of a single precipitate computed with anisotropic, homogeneous elasticity. The chemical potentials are plotted along a horizontal slice through the center of the particle ($y = \pi$). This simulation will be described in greater detail in Section 6 (see Fig. 3). Here, we note that algorithm A is used in this simulation. In Fig. 1(a), the upper curve corresponds to $\gamma = 0.15$ and $\Delta t = 3 \times 10^{-6}$ and in the lower curve, $\gamma = 0.075$ and $\Delta t = 7.5 \times 10^{-7}$. The grid size is $h_1 = h_2 = 2\pi/256$. The dashed and dotted curves correspond to the true chemical potential while the solid curves correspond to the modified chemical potential. The oscillations observed in the true chemical potential occur at the interface layers and are a result of the time-step dependent smoothing of the small scales present in these layers. In contrast, the modified chemical potentials are constant to four digits. This constant depends on γ, for $\gamma = 0.15$, $\mu^* = 1.319$ while for $\gamma = 0.075$,

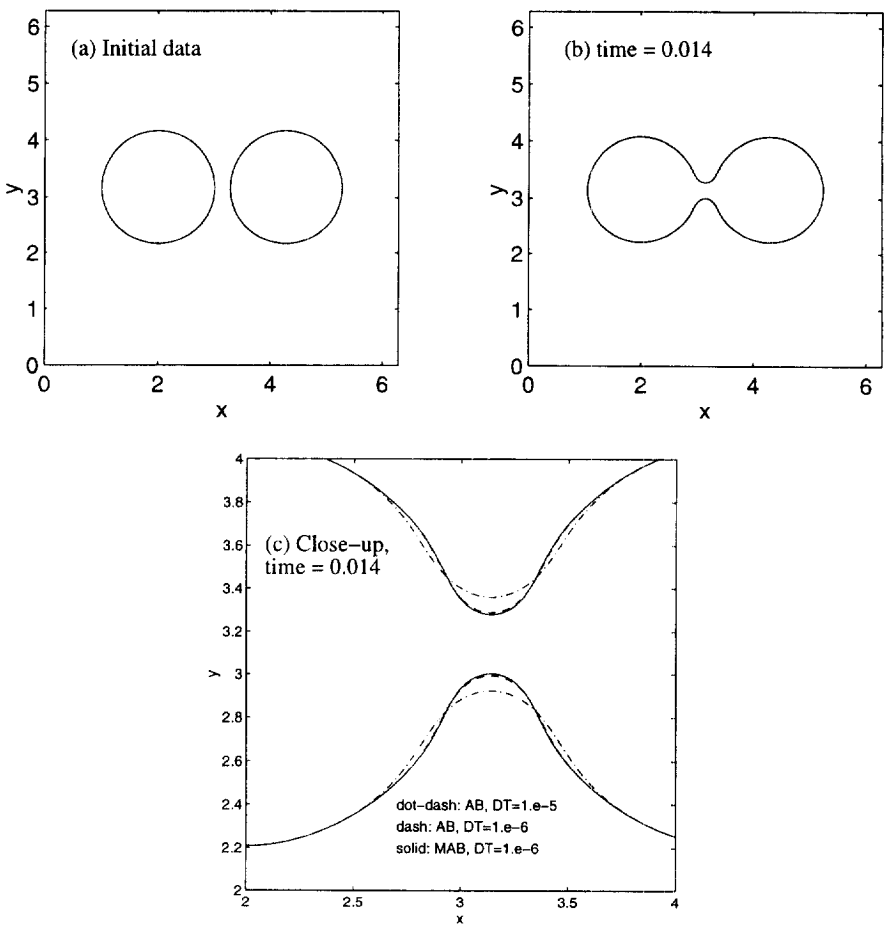

Fig. 2. Merging of two soft precipitates. (a) Initial; (b) final 0.5 composition contours using algorithm B ($\Delta t = 1 \times 10^{-6}$); (c) comparision of 0.5 composition contours for algorithm A and B, dot–dashed curve: algorithm A with $\Delta t = 1 \times 10^{-5}$, dashed curve: algorithm A with $\Delta t = 1 \times 10^{-6}$, solid curve: algorithm B with $\Delta t = 1 \times 10^{-6}$. The elasticity is isotropic, inhomogeneous with $Z = 2.7$, $G^P = 0.5$ and dilatational misfit. The spatial grid spacing is $h_1 = h_2 = 2\pi/256$.

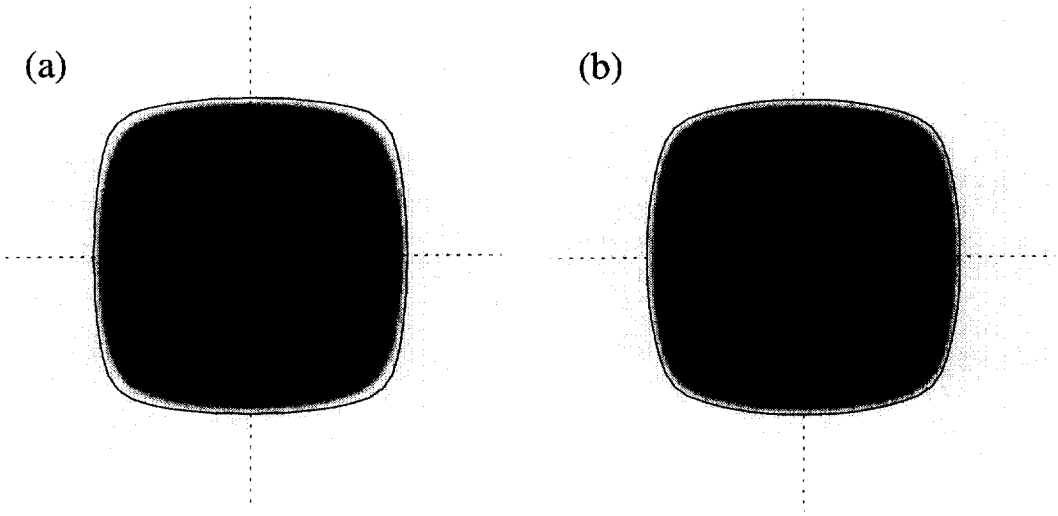

Fig. 3. Comparison of DI and BI precipitate shapes for cubic anisotropic, homogeneous media. DI shapes are the same in (a) and (b). In (a), an infinite far-field boundary is used for the BI calculation. In (b), periodic boundary conditions are simulated for the BI calculation. The elastic parameters and the spatial grid size are the same as in Fig. 1 and $\Delta t = 3 \times 10^{-6}$.

$\mu^* = 0.677$. This indicates a linear dependence on γ consistent with the sharp interface asymptotics.

One can improve the agreement between the true and modified chemical potentials by taking very small time steps. However, this quickly becomes impractical. Indeed, an important question at this point is whether these differences result in observable changes at the macroscopic level such as equilibrium particle shapes and curvatures or the dynamics of topological transitions. To answer question, one can develop time stepping algorithms that yield the correct equilibrium μ = constant and then compare the results to those of algorithm A. While standard Crank–Nicholson methods yield this correct equilibrium, the time steps required for stability are impractically small, as noted above. Instead, we have developed a modified Adams–Bashforth method as follows:

$$\hat{c}^{n+1} = \left[1 - \frac{\gamma}{2} e^{-\gamma |k|^4 \Delta t}(3 - e^{-\gamma |k|^4 \Delta t})\right] \hat{c}^n - \frac{\Delta t}{2} \frac{|k|^2}{\gamma} e^{-\gamma |k|^4 \Delta t}(3\hat{\mathcal{N}}^n - e^{-\gamma |k|^4 \Delta t} \hat{\mathcal{N}}^{n-1}). \quad (42)$$

This method, referred to as algorithm B, is second order accurate in time, leads to the correct equilibrium and has good stability properties, although it does require time steps an order of magnitude smaller than those needed for algorithm A.

In Fig. 1(b), comparisons are presented for the true chemical potentials using algorithms A and B. The situation is the same as in Fig. 1(a) with $\gamma = 0.15$ and $\Delta t = 1 \times 10^{-7}$. As was observed in Fig. 1(a), the chemical potential from algorithm A exhibits oscillations at the interface layers. These oscillations are removed by using algorithm B (the solid line in Fig. 1(b)). Interestingly, the true chemical potential from algorithm B differs from the modified chemical potential from algorithm A only in the sixth digit.

We close this Section by considering the dependence of macroscopic quantities on the two algorithms A and B. In other words, do the oscillations observed in the true chemical potential affect the particle shapes or dynamics? As will be shown in the next two figures, the answer appears to be no. In Fig. 1(c), we consider the curvature of the $c = 0.5$ contour line for a single precipitate. Two curvatures are shown corresponding to the results from algorithms A and B. The conditions for the precipitate are the same as in Fig. 1(a) and (b) except that the result from algorithm A uses the time step $\Delta t = 5 \times 10^{-6}$. The curvatures are plotted as functions of a scaled arclength parameter. Clearly, the curvatures are very similar. Even at the high curvature corners the curvatures differ by only 5%. This is significant because the $c = 0.5$ contour lies inside the interface layer where oscillations are observed for the true chemical potential from algorithm A.

Similar conclusions can be reached in the context of topological transitions. In Fig. 2, we show the merging of two precipitates in the setting of isotropic, inhomogeneous elasticity. The physical situation is the same as in Fig. 6, described in detail in Section 6, except that the particles are placed closer to each other initially (Fig. 2(a) shows the initial $c = 0.5$ contour line). In Fig. 2(b), the $c = 0.5$ contour line is shown after the precipitates have merged. This figure was generated using algorithm B using $\Delta t = 1 \times 10^{-6}$. Figure 2(c) shows a close-up

of the neck region at the same time. Results are shown using algorithms A and B with $\Delta t = 1 \times 10^{-6}$ and algorithm A with $\Delta t = 1 \times 10^{-5}$. We note that the only differences in the results are in the neck region and are primarily due to the time step chosen. Moreover, the time of merging appears to be independent of the algorithm.

Overall, we conclude that the time stepping algorithm A is robust and accurately captures macroscopic features such as equilibrium particle shapes and curvatures and the dynamics of topological transitions. However, to accurately capture fine details such as the chemical potential through the interface layer, one should use algorithm B. Since larger time steps can be used with algorithm A and we are interested primarily in macroscopic quantities, we will use algorithm A for the simulations in the remainder of this paper.

6. RESULTS

6.1. Numerical comparison of the models

We now compare results from the sharp and diffuse interface models. We identify the primary differences in the results as being due to: (1) an infinite far-field boundary (sharp) vs periodic boundary conditions (diffuse), (2) the value of γ used in the diffuse interface model and (3) one-sided diffusion (sharp) vs two-sided diffusion (diffuse). We illustrate the first two through a series of comparisons below. Later, we present a calculation in which the two-sided diffusion becomes important.

We consider first the evolution of a single precipitate in an anisotropic, cubic, homogeneous elastic medium with elastic constants $C_{11} = 1.98$ and $C_{12} = 1.18$ which are appropriate for Ni–Al alloys (see [14]). The misfit strain $\mathcal{E}^T$ is dilatational. It is well known [14] that in this situation, the equilibrium shape is squarish, and is characterized by the dimensionless parameter Z. Figure 3(a) and (b) show the $Z = 8$ equilibrium shape from both the boundary integral calculation (solid line) and the grey scale composition contours from the diffuse interface simulation with $\gamma = 0.15$. The DI results are the same in both graphs. The BI calculation shown in Fig. 3(a) is for an isolated particle in an infinite matrix. In contrast, the BI the calculation in Fig. 3(b) is for a particle that has been surrounded by nine identical particles, in order to simulate the periodic boundary conditions used in the DI calculation. The initial precipitate shape for both simulations is a circle with radius equal to 2 and for the diffuse model, $c = 1$ inside the precipitate and $c = 0$ outside so that initially, the boundary is sharp.

In both cases, there is qualitative agreement between the BI and DI shapes, though the diffuse shape is slightly smaller than the BI shapes. This reduction in area is related to the choice of γ. Figure 4(a) shows a plot of area vs time for the DI simulations with $\gamma = 0.15$ and $\gamma = 0.075$, as well as for the BI simulation. The area is constant in the BI approach [12]. For the diffuse shapes, area is defined as the area inside the $c = 0.5$ contour line. Since the initial precipitate for the diffuse model has a sharp boundary, there is a rapid initial drop-off of the area, as the transition region equilibrates and becomes diffuse. As γ decreases and the transition region becomes thinner, less area is lost compared to the BI result and we find approximately linear convergence to the BI area with decreasing γ. This is consistant with our asymptotic results in Section 4.

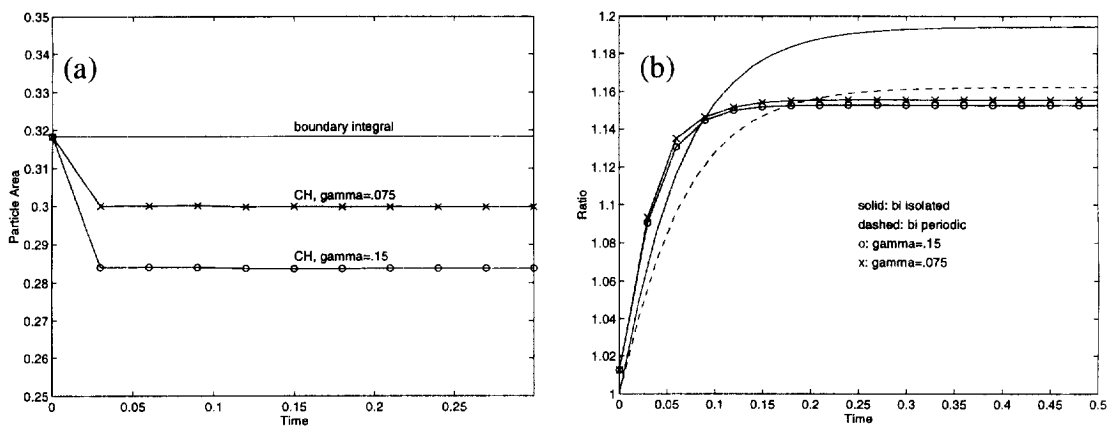

Fig. 4. Evolution of precipitate area and diagonal–horizontal ratio. (a) Precipitate area, x denotes $\gamma = 0.075$, o denotes $\gamma = 0.15$. (b) Diagonal–horizontal ratio, solid curve: BI calculation with infinite far-field boundary, dashed curve: BI calculation with simulated periodic boundary conditions, o denotes $\gamma = 0.15$, x denotes $\gamma = 0.075$. Parameters are the same as Fig. 3. For the BI simulation, $N = 64$ grid points and $\Delta t = 1 \times 10^{-3}$.

A close examination of Fig. 3(a) also reveals that the diffuse shape is "rounder" than the BI shape. This can be quantified by calculating the ratio of diagonal length to horizontal length for the particles, as shown in Fig. 4(b). Note that the BI calculation for the isolated particle produces a significantly "squarer" (larger diagonal/horizontal ratio) than the BI calculation with the simulated periodic boundary conditions. Also, we observed that for the diffuse shapes, the diagonal/horizontal ratio increases as γ decreases, and appears to be converging to the BI result with periodic boundary conditions.

A second example of the influence of boundary conditions is shown in Fig. 5. In this calculation, we again assume cubic anisotropic, homogeneous elasticity with the same elastic constants and Z as in Fig. 3. Here, we consider two initially circular particles whose centers are initially aligned along the ⟨11⟩ direction (inset Fig. 5). As in Fig. 3, the initial particle boundaries in the DI simulation are sharp. We show these particles at dimensionless time 1.0 for both the BI and DI simulations. The DI shape is the same in both Fig. 5(a) and (b). The BI result in Fig. 5(a) corresponds to two isolated particles, while in Fig. 5(b), we simulate periodic boundary conditions as described above. In both cases, we observe that the particles align in the soft ⟨10⟩ direction with an apparently stable interparticle distance. This has been seen in previous simulations [16]. We find again much better agreement between the DI results and the BI results with simulated periodic boundary conditions.

We have also found good agreement between DI and BI results for the case of isotropic, inhomogeneous elasticity. Figure 6 shows a DI and BI simulation of two "soft" particles with $G^P = 0.5$ (recall $G^M = 1$), $Z = 2.7$ and with dilatational misfits. By soft, we mean that the shear modulus of the precipitate is less than that of the surrounding matrix. The Poisson ratios are $\nu^M = \nu^P = 0.2$. The precipitates are initially circular with radius 1 and have sharp boundaries (see inset). The BI calculation was performed for two isolated particles. The particle shapes resulting from the two models are qualitatively similar, though the interacting tips are much sharper in the BI simulations. However, the BI simulation breaks down as the precipitates merge. The DI model, on the other hand, naturally handles the expected merging of the two particles (see Fig. 7). The sharpness of the interacting tips in the DI simulation can be increased by decreasing γ. The specific choice of γ has a strong effect on the time at which the particles merge, such that decreasing γ delays merging; however, it has very little effect on the evolution either prior to or after merging. Finally, we remark that since the main elastic interactions are between the two particles, there is essentially no difference between BI calculations with isolated particles and with simulated periodic boundary conditions as above.

The BI calculations presented above are much cheaper to perform than the DI simulations. Both sets of results were obtained using the Cray C90; the BI simulations required approximately 0.05–0.25 h to complete while the DI calculations required 1–2 h. The precise numerical parameters can be found in the figure captions. Notably, the DI simulations used the spatial grid size $h_1 = h_2 = 2\pi/256$ which yields approximately 16

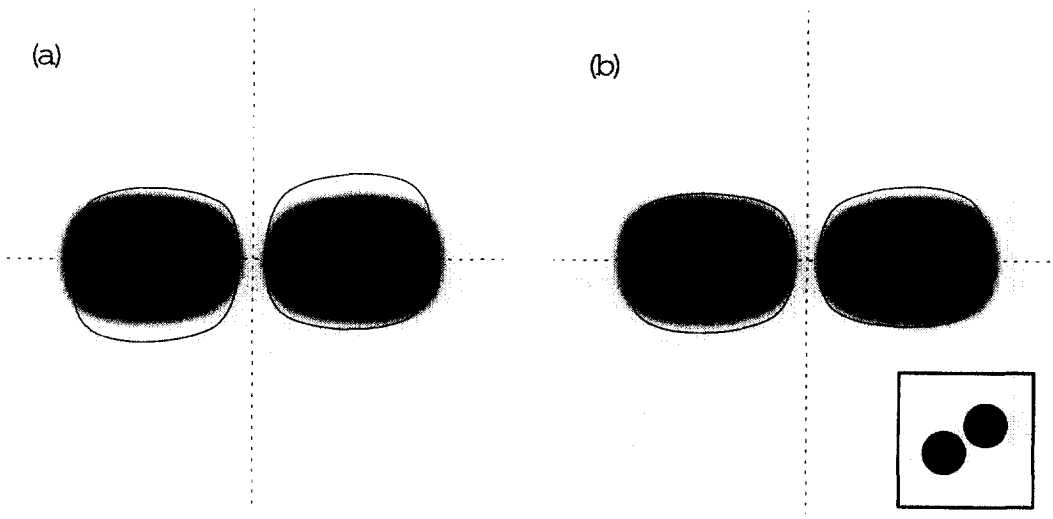

Fig. 5. BI/DI comparisons for two translating precipitates. The DI results are the same in each figure. (a) The BI calculation with infinite far-field boundary. (b) The BI calculation uses simulated periodic boundary conditions. The inset shows the initial condition. The elastic parameters are as in Fig. 3 with $Z = 4$. For the DI model, $h_1 = h_2 = 256$ and $\Delta t = 5 \times 10^{-6}$. For the BI model, $N = 64$ on each interface and $\Delta t = 1 \times 10^{-3}$.

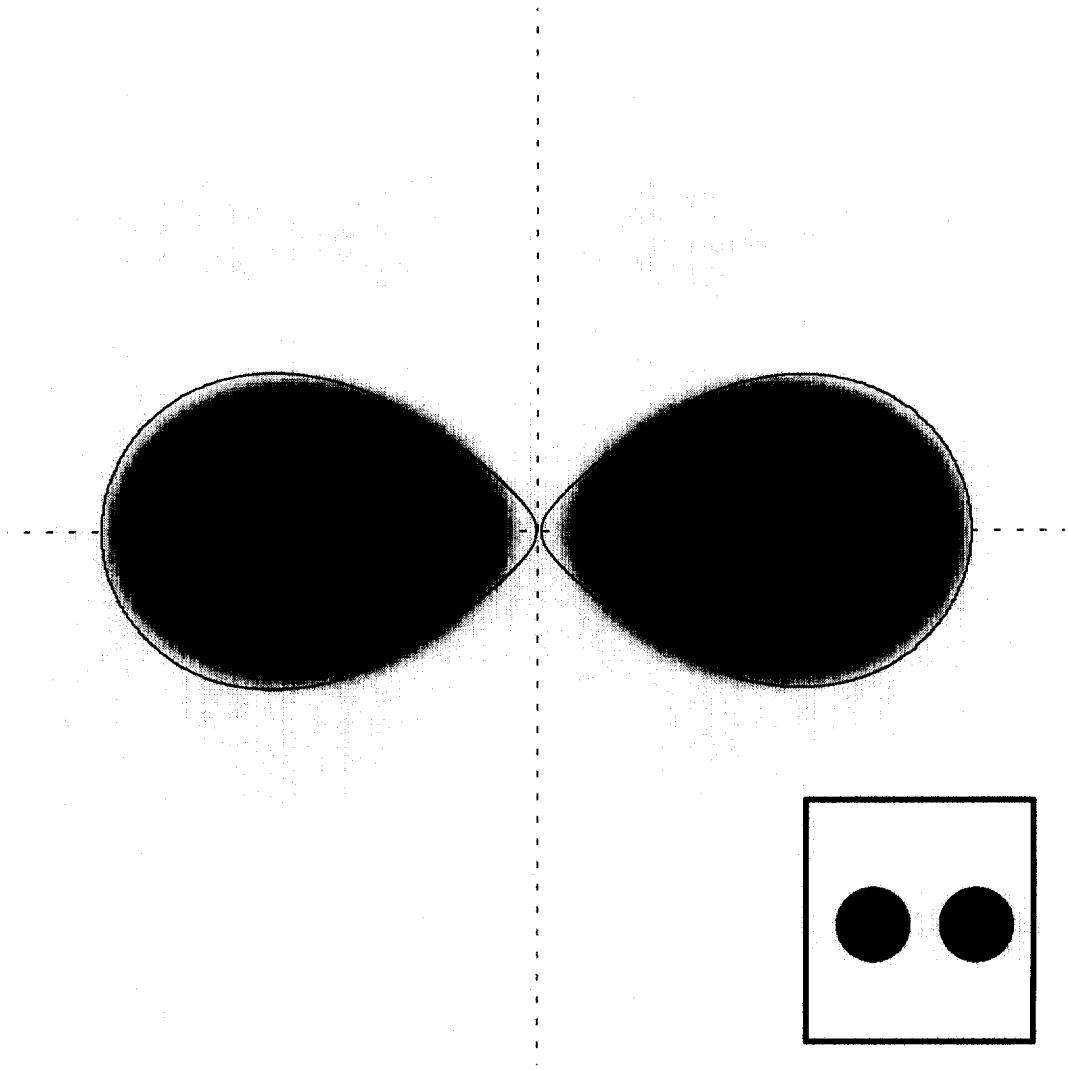

Fig. 6. BI/DI comparisons for two merging precipitates. The initial condition is shown in the inset. The elastic parameters are the same as in Fig. 2. The parameters for the DI model are the same as for the dot–dashed curve in Fig. 2. For the BI model, $N = 512$ on each interface and $\Delta t = 5 \times 10^{-3}$.

grid points across the interface layer when $\gamma = 0.15$. The time step for the DI simulations ranged from $O(10^{-6})$ for the results in the homogeneous, cubic anisotropic elastic medium to $O(10^{-5})$ for the inhomogeneous, isotropic medium.

6.2. *Inhomogeneity effects and topological transitions*

We now consider the role that elastic *inhomogeneity* plays in microstructural evolution. One of the interesting consequences of elastic inhomogeneity is its effect on particle–particle attraction or repulsion. In an isotropic, inhomogeneous medium where there is a dilatational misfit, precipitates with shear modulus $G^P > 1$ (referred to as "hard" precipitates) tend to repel one another while those with $G^P < 1$ ("soft" precipitates) tend to attract [12, 24]. This is in striking contrast with the case of homogeneous, cubic anisotropic medium in which a stable interparticle distance is observed [16]. Compare the results in Fig. 5(a) or (b) with those in Fig. 6.

In this section, we focus only on the DI model while examining the effect of inhomogeneity and the dynamics of topological transitions. Unless otherwise stated, the misfit is taken to be dilatational. The precise numerical parameters can be found in the figure captions.

In Fig. 7, we present a continuation of the simulation involving the two soft precipitates shown in Fig. 6. The merging is captured smoothly and the resulting single precipitate evolves toward a circular shape. This circular equilibrium shape is a reflection of the analysis of Johnson and Cahn [36] which pre-

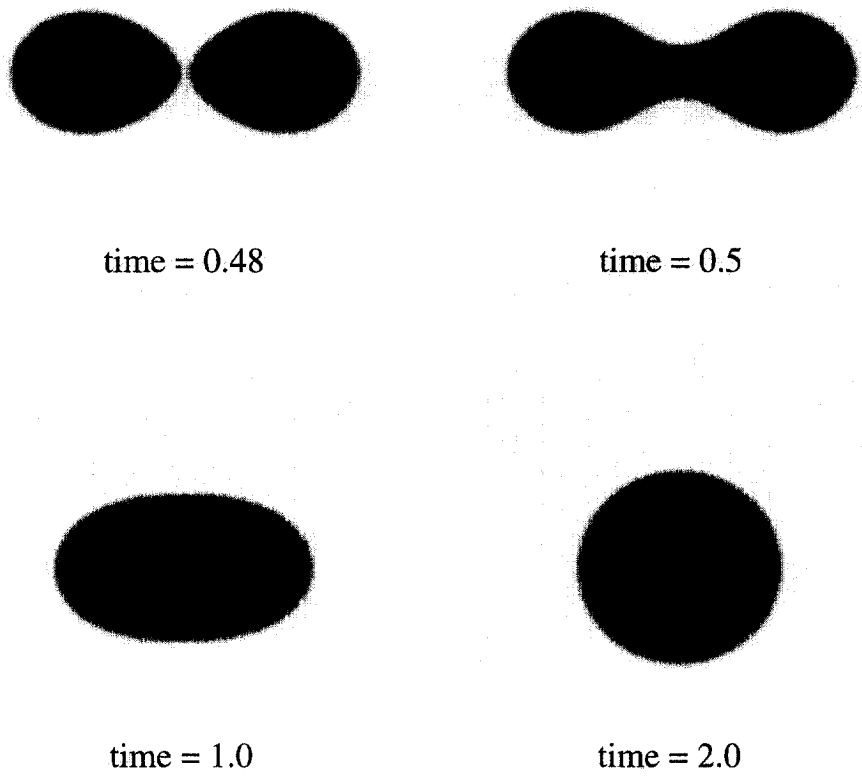

Fig. 7. Merging of two precipitates. This is a continuation of the DI calculation shown in Fig. 6. The final time $t = 2.0$ shows the equilibrium microstructure.

dicts that the equilibrium shape of a single soft particle is circular for the values of the material constants we used here. In [36], Johnson and Cahn derive a bifurcation parameter between circular and elliptical precipitate shapes, which depends on the area of the precipitates, the elastic constants, the misfit and the surface energy. Using $\nu^M = \nu^P = 0.2$ and $G^P = 0.5$, this parameter can be reduced to our parameter Z. Johnson and Cahn showed that there is a critical value $Z_{crit} = 4.76$ such that for $Z < Z_{crit}$, circular equilibrium shapes are observed while for $Z > Z_{crit}$, elliptical equilibrium shapes are seen. Recall that in Fig. 7, $Z = 2.7$.

If Z is increased above Z_{crit}, we still expect particle attraction and merging, but the single merged particle should become ellipsoidal. This is seen in Fig. 8 where we show two equilibrium shapes after merging. The initial precipitate shapes and the misfit are as in Fig. 6. In Fig. 8(a), $Z = 5.4$ while in Fig. 8(b), $Z = 10.8$. The primary differences in the evolution among the simulations with $Z = 2.7$, 5.4 and 10.8 occur after merging. We remark that we find excellent agreement with the Johnson–Cahn result even though arbitrary shapes are allowed in our approach.

It is interesting to follow the evolution of the system energy $E(t)$, from equation (10), throughout the merging process. In Fig. 9, $E(t)$ is plotted for the simulations in Figs 7 and 8. In each of these energies, the rapid drop marks the precipitate merging. The sharp corners in the curves are due to the fact that the energy is plotted every 0.02 time-units while the transitions occur more rapidly. In fact, $E(t)$ varies smoothly with t. Note that the merging occurs at earlier times as Z is increased. This behavior is the characteristic signature of topological transitions in the DI model. In the BI model, [12] showed that $dE/dt \to -\infty$ at a topological transition. Here, we note that dE/dt is a negative finite number because the interfaces are diffuse.

We consider next the evolution of four precipitates. We begin by taking hard particles ($G^P = 2.0$, $\nu^P = \nu^M = 0.2$, $Z = 2.7$). In this case the interparticle forces are repulsive, such that in the absence of a

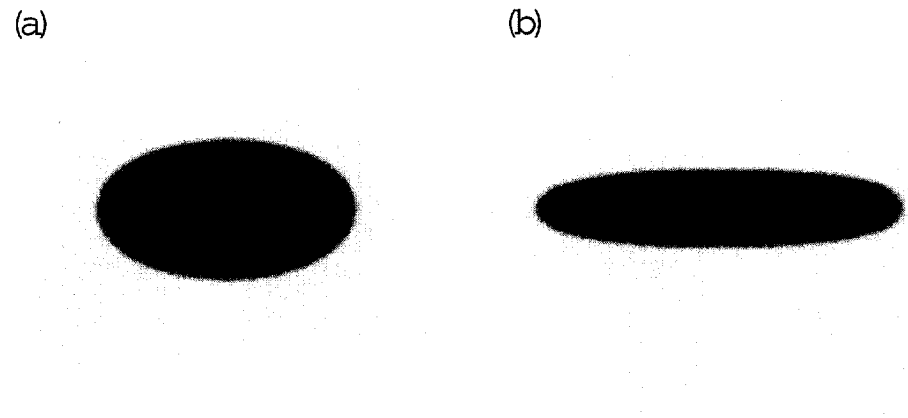

Fig. 8. Equilibria of two merged precipitates. The elastic parameters are the same as in Fig. 2. The spatial grid spacing is $h_1 = h_2 = 256$. (a) $Z = 5.4$ and $\Delta t = 1 \times 10^{-5}$, (b) $Z = 10.8$ and $\Delta t = 5 \times 10^{-6}$.

far-field boundary, the precipitates would move infinitely far from each other [12]. Here, a finite outer boundary is effectively imposed by the periodic boundary conditions and so an equilibrium particle configuration is reached in each periodic cell. The initial and final configurations are shown in Fig. 10. The initial particles are symmetrically placed and have sharp boundaries. Note that at the final time, the boundaries of neighboring precipitates are relatively flat due to the repulsive forces.

We now turn to the evolution of four soft precipitates ($G^P = 0.5$, $\nu^P = \nu^M = 0.2$, $Z = 9.6$); this displays much more interesting dynamics than the hard precipitate case considered above. The initial condition is the same as in Fig. 10. The evolution of the precipitates is shown in Fig. 11. We observe that the precipitates merge both horizontally and vertically, so that the soft material completely surrounds a hard matrix center. Similar coating of

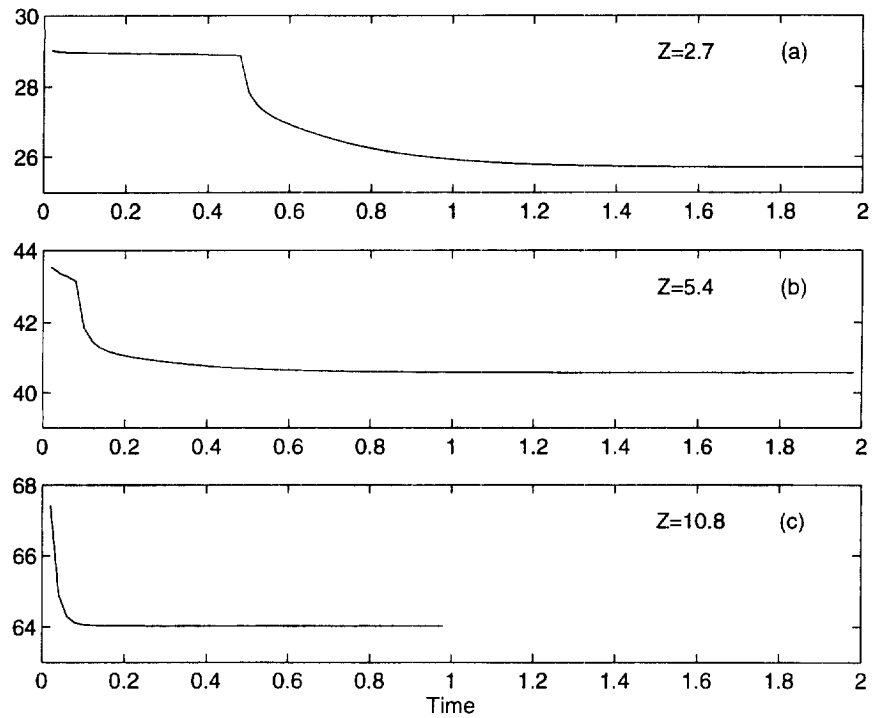

Fig. 9. Total energy of merging precipitate system. (a) $Z = 2.7$ from Fig. 7. (b) $Z = 5.4$ from Fig. 8(a). (c) $Z = 10.8$ from Fig. 8(b).

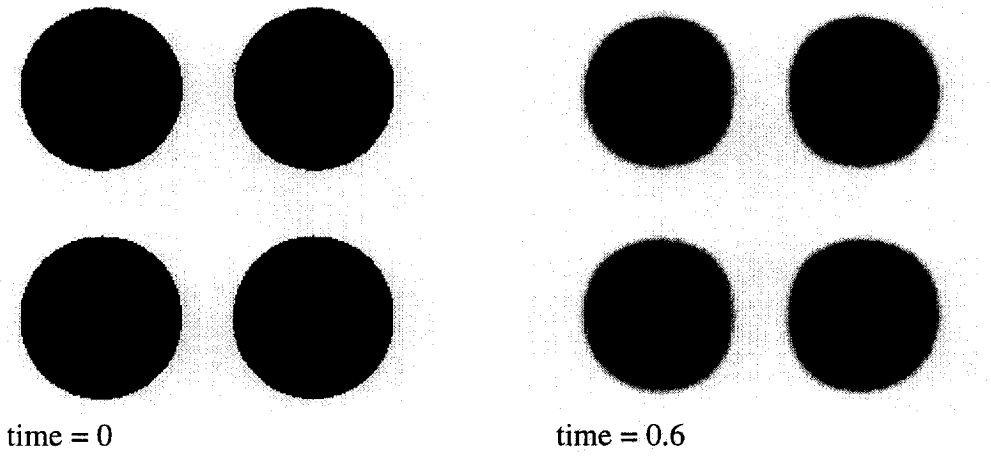

Fig. 10. Four symmetrically-placed hard precipitates. Initial and final times are shown. The elasticity is isotropic, inhomogeneous with $Z = 2.7$, $G^P = 2$ and the misfit is dilatational. The spatial grid size is $h_1 = h_2 = 2\pi/256$ and $\Delta t = 2.5 \times 10^{-6}$.

elastically hard material with elastically softer material has been observed by Lee [37].

However, in our simulations, the hard center that is formed at early times eventually diffuses out through the soft annulus, leaving a single soft particle. This soft particle continues to evolve until it forms a cross that connects with its periodic images. This gives a final configuration where the phases have reversed roles—hard particles surrounded by a soft matrix. This microstructure is stable, and is

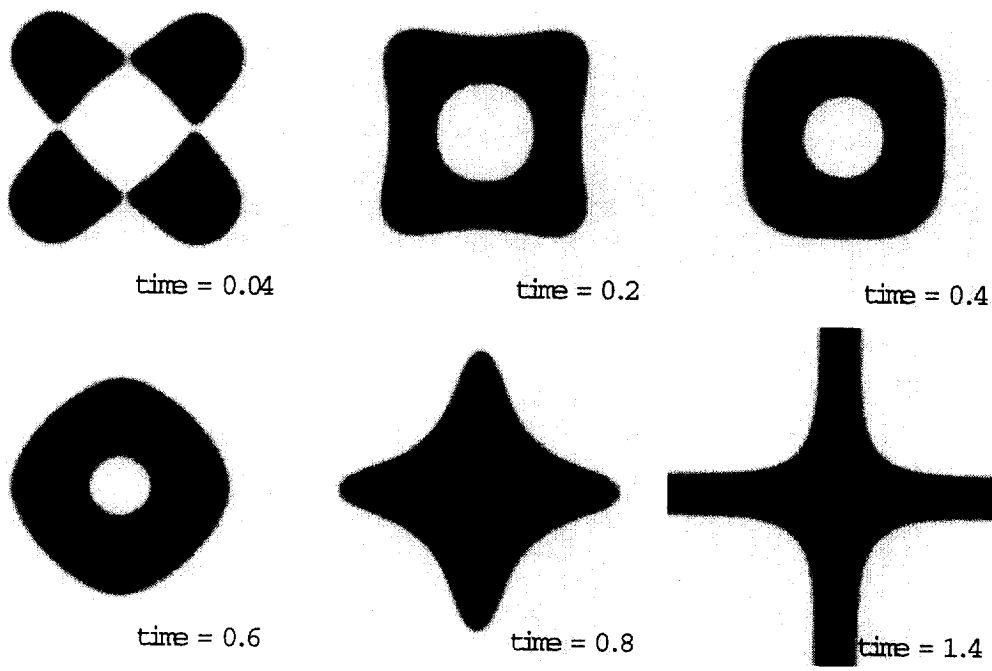

Fig. 11. Evolution of four symmetrically-placed soft precipitates. The elastic parameters are the same as in Fig. 2 with $Z = 9.6$. The initial condition is the same as in Fig. 10. The spatial grid size is $h_1 = h_2 = 2\pi/256$ and $\Delta t = 5 \times 10^{-6}$. This figure shows the transition from soft precipitates/hard matrix to a microstructure with hard precipitates/soft matrix.

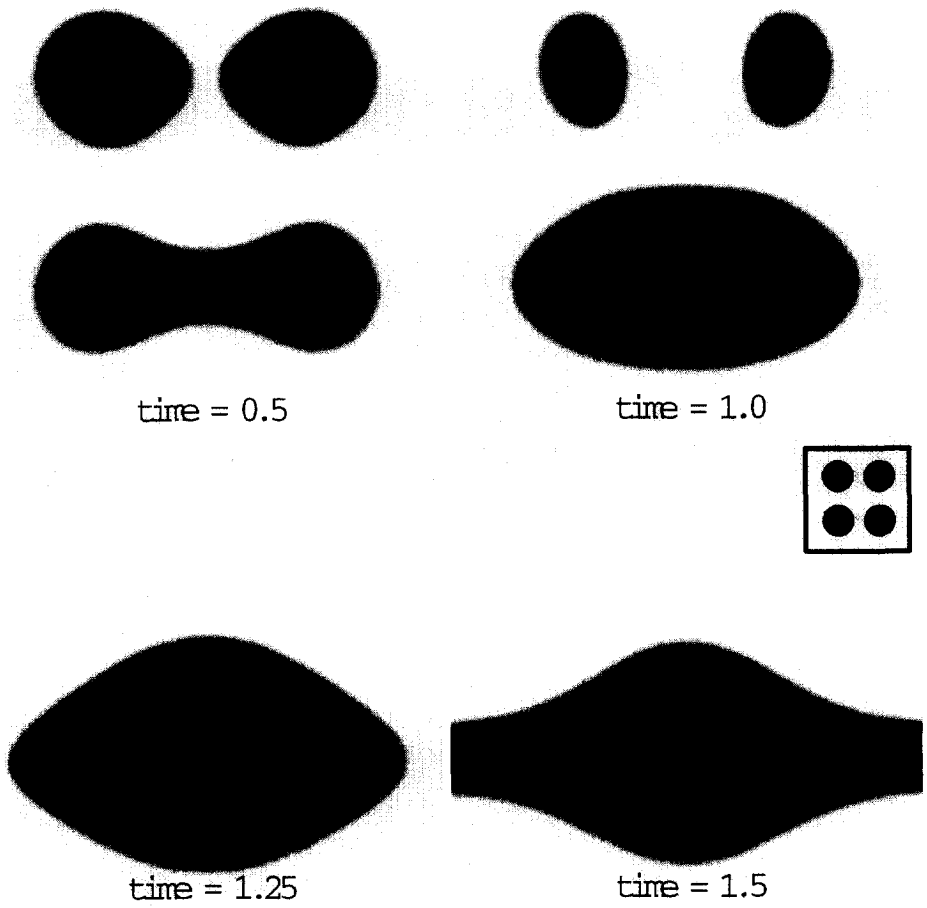

Fig. 12. Evolution of four asymmetrically-placed soft precipitates. The elastic parameters are the same as in Fig. 2 with $Z = 5.4$. The initial condition is shown in the inset. The spatial grid size is $h_1 = h_2 = 2\pi/256$ and $\Delta t = 1 \times 10^{-5}$. This figure shows the microstructure evolving from precipitates to plates.

consistent with both elastic energy calculations [38, 39] and calculations of the effective moduli of composite materials [40]. Moreover, it is the two-sided diffusion in the DI model that provides the mechanism by which the coated microstructure (times 0.2–0.6) continues to evolve toward a lower energy state. In this case, relaxing the constraint of one-sided diffusion seems to have important consequences on the equilibrium microstructure.

We find that both the dynamics and the final structures computed from the DI method are strongly dependent on the initial condition and the periodic boundary conditions. For example, Fig. 12 shows the evolution of four soft precipitates; the parameters are the same in Fig. 11 except that $Z = 5.4$ and initially, the upper particles are closer to the top boundary of the periodic box than to the lower particles (see inset). This breaks the symmetry of the calculation such that the lower particles coarsen at the expense of the upper ones. Concurrent with this coarsening, the bottom particles merge, lengthen and eventually merge with their periodic images. After $t = 1.5$, the sides of the structure flatten and the equilibrium configuration is a horizontal plate (not shown).

We conclude by showing two calculations of the evolution of 12 particles. In Fig. 13, the particles are harder than the matrix ($G^P = 2.0$) while in Fig. 14 they are softer ($G^P = 0.5$). In both cases, the same initial data is used (see insert). $\nu^M = \nu^P = 0.2$, $Z = 1.2$ and there is a tetragonal misfit $\mathcal{E}^T_{11} = 1$, $\mathcal{E}^T_{22} = 2$, $\mathcal{E}^T_{12} = 0$, recall that the scaling of the misfit is contained in Z). In both the hard and soft particle simulations, we observe that the final microstructure consists of a single particle. In fact, we were unable to find any evidence of elastic stabilization of a multidisperse microstructure in any simulation. Because of the tetragonal misfit, the coarsened particle is an ellipse in the hard case (Fig. 13(f)), and plate-like in the soft case (Fig. 14(f)). While we do

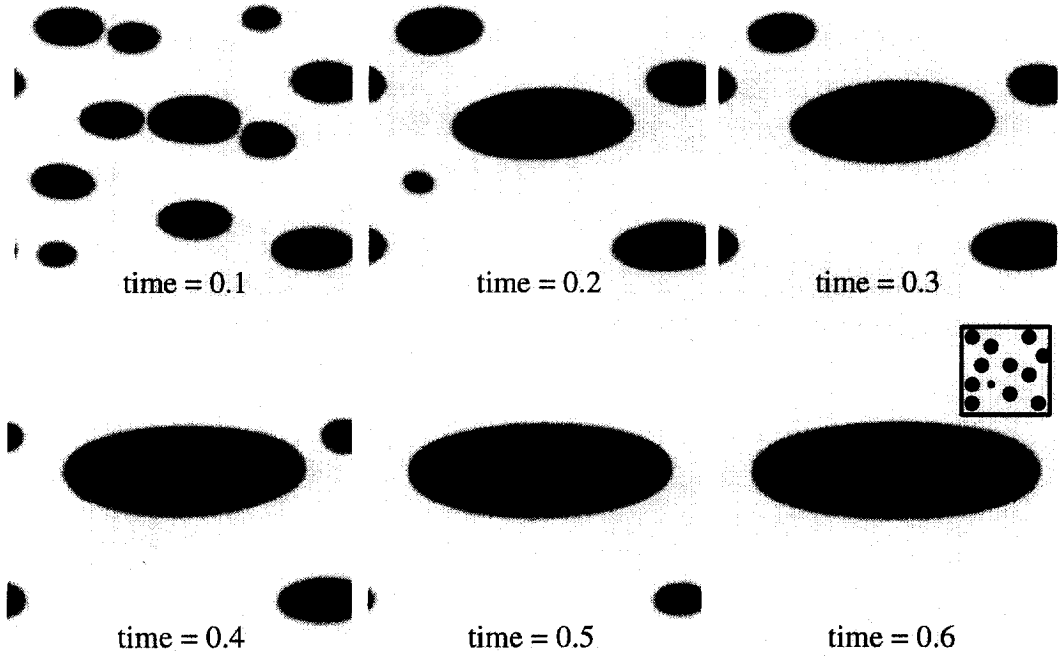

Fig. 13. Coarsening of 12 hard precipitates. The initial configuration is shown in the inset. The elastic parameters are the same as in Fig. 10 except that $Z = 1.2$ and the misfit is tetragonal $\mathcal{E}^{T}_{11} = 1$, $\mathcal{E}^{T}_{22} = 2$ and $\mathcal{E}^{T}_{12} = 0$. The spatial grid size is $h_1 = h_2 = 2\pi/256$ and $\Delta t = 5 \times 10^{-6}$. The resulting equilibrium consists of an elliptical particle.

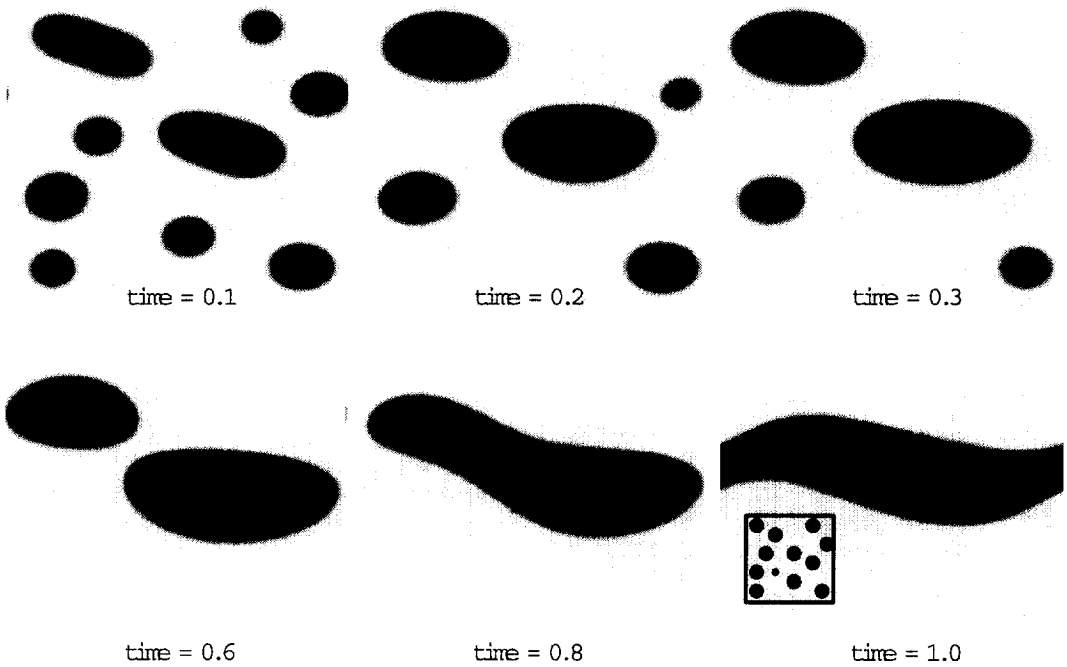

Fig. 14. Coarsening of 12 soft precipitates. The initial configuration is shown in the inset and is the same as in Fig. 13. The elastic parameters are the same as in Fig. 13 except that $G^{P} = 0.5$. The space and time grid sizes are the same as in Fig. 13. The resulting equilibrium consists of a plate-like particle.

not have enough particles to form statistically significant conclusions about the overall kinetics of the process, we find that the overall coarsening kinetics in the two cases are qualitatively similar. However, the detailed kinetics are different in the two cases. In the hard case (Fig. 13), the kinetics are dominated by "classical" coarsening and there is little merging of particles. In contrast, in the soft case (Fig. 14), at early times, there is rapid particle merging between closely-spaced particles. At later times, the resulting well-separated particles coarsen.

7. SUMMARY

In this paper, we study the diffusional evolution of microstructure in elastic media in two dimensions using both a sharp interface and a diffuse interface model. In the former, the matrix-precipitate interfaces are assumed to be sharp and diffusion only takes place in the matrix phase. In the latter, the interfaces are given a finite but small thickness and a set of partial differential equations is used to model the evolution in the entire multi-phase domain.

We present theoretical and numerical results comparing the two approaches in isotropic, inhomogeneous *and* in anisotropic, homogeneous elastic media. These choices are motivated by the fact that there are well-developed methods for solving the sharp interface system in these situations [12, 15]. From the theoretical point of view, we use the method of matched asymptotic expansions to show that as the width of the interface layer in the diffuse model is taken to zero, the diffuse equations converge to a sharp interface system in the limit. This limiting system has diffusion in both the matrix and precipitate (two-sided diffusion) but otherwise matches the original sharp interface system.

To solve the diffuse interface system numerically, we develop a pseudo-spectral method using periodic boundary conditions. We use a nonstiff updating scheme in time (algorithm A) and carefully investigate its effect on both equilibrium and evolving precipitate shapes. We show that while algorithm A is robust, it can lead to equilibria in which details, such as the chemical potential, depend sensitively on the small scales present in the solution. However, we show that *macroscopic* features (e.g. precipitate shape, curvature) are captured by algorithm A.

Finally, we use the diffuse interface approach to study the effect of elastic inhomogeneity and topological transitions on microstructural evolution. We find, as in [12, 24], that precipitates with dilatational misfits and a higher shear modulus than the matrix tend to repel one another through their elastic interaction. In contrast, precipitates with a lower shear modulus than the matrix tend to attract. This leads to particle merging which is captured smoothly using the diffuse interface model. We find that the evolution process and resulting equilibrium microstructure depends strongly on the initial data and the periodic boundary conditions. We also give an example where the two-sided diffusion in the diffuse interface model has important consequences on the equilibrium microstructure. In a forthcoming work we will consider the effects of both elastic anisotropy and inhomogeneity on microstructural evolution using sharp and diffuse interface models.

Acknowledgements – We wish to thank R. V. Kohn, Q. Nie, M. J. Shelley and P. Voorhees for interesting discussions concerning this work. We gratefully acknowledge the support of the Minnesota Supercomputer Institute. In addition, this work is partially supported by National Science Foundation grants CMS-9503393 (PHL) and DMS-940310 (JSL), and the Sloan foundation (JSL).

REFERENCES

1. Ardell, A. J. and Nicholson, R. B., *Acta metall.*, 1966, **14**, 1295.
2. Miyazaki, T., Hakamura, K. and Mori, H., *J. Mater. Sci.*, 1979, **14**, 1827.
3. Imamura, H., Miyazaki, T. and Kozakai, T., *Mater. Sci. Eng.*, 1982, **54**, 9.
4. Maheshwari, A. and Ardell, A. J., *Phys. Rev. Lett.*, 1993, **70**, 2305.
5. Yoo, Y. S., Yoon, D. Y. and Henry, M. F., *Metals Mat.*, 1995, **1**, 47.
6. Cahn, J. W. and Hilliard, J. E., *J. Chem. Phys.*, 1958, **28**, 258.
7. Cahn, J. W., *Acta metall.*, 1961, **9**, 795.
8. Gurtin, M. E., *Physica D*, 1996, **92**, 178.
9. Johnson, W. C., *Metall. Trans.*, 1987, **18A**, 233.
10. Johnson, W. C., Voorhees, P. W. and Zupon, D. F., *Metall. Trans.*, 1989, **20A**, 1175.
11. Johnson, W. C., Abinandanan, T. A. and Voorhees, P. W., *Acta metall.*, 1990, **38**, 1349.
12. Jou, H.-J., Leo, P. H. and Lowengrub, J. S., *J. Comp. Phys.*, 1997, **131**, 109.
13. Socrate, S. and Parks, D. M., *Acta metall.*, 1993, **41**, 2185.
14. Thompson, M. E., Su, C. S. and Voorhees, P. W., *Acta metall.*, 1994, **42**, 2107.
15. Su, C. H. and Voorhees, P. W., *Acta mater.*, 1996, **44**, 1987.
16. Su, C. H. and Voorhees, P. W., *Acta mater.*, 1996, **44**, 2001.
17. Voorhees, P. W., Boisvert, R. F., McFadden, G. B. and Meiron, D. I., *Acta metall.*, 1988, **36**, 207.
18. Voorhees, P. W., McFadden, G. B. and Johnson, W. C., *Acta metall.*, 1992, **40**, 2979.
19. Khachaturyan, A. G., Semenovskaya, S. V. and Morris, J. W. Jr, *Acta metall.*, 1988, **36**, 1563.
20. McCormack, M., Khatchaturyan, A. G. and Morris, J. W. Jr, *Acta metall.*, 1992, **40**, 325.
21. Wang, Y., Chen, L. Q. and Khachaturyan, A. G., *Acta metall.*, 1993, **41**, 279.
22. Wang, Y. and Khachaturyan, A. G., *Acta metall.*, 1995, **43**, 1837.
23. Lee, J. K., *Scr. Met.*, 1995, **32**, 559.
24. Lee, J. K., *Metall. Trans. A*, 1996, **27**, 1449.
25. Eshelby, J. D., *J. Elast.*, 1975, **5**, 321.
26. Eshelby, J. D., in *Progress in Solid Mechanics*, 2 edn, ed. I. N. Sneddon and R. Hill, North-Holland, Amsterdam, 1961, p. 89.
27. Fried, E. and Gurtin, M. E., *Physica D*, 1994, **72**, 287.
28. Fried, E. and Grach, G., *Arch. Rat. Mech.*, to appear.
29. Thompson, M. E. and Voorhees, P. W., preprint.

30. Gurtin, M. E. and McFadden, G. B., in *IMA Series in Mathematics and its Applications*, Vol. 43. Springer-Verlag, New York, 1992.
31. Pego, R., *Proc. R. Soc. London A*, 1989, **422**, 261.
32. Penrose, O. and Fife, P. C., *Physica D*, 1990, **43**, 44.
33. McFadden, G. B., Wheeler, A. A., Braun, R. J., Coriell, S. R. and Sekerka, R. F., *Phys. Rev. E*, 1993, **48**, 2016.
34. Leo, P. H., Lowengrub, J. S. and Jou, H.-J., Minnesota Supercomputer Institute, preprint.
35. Stoer, J. and Burlisch, R., *Introduction to numerical analysis*, Springer Verlag, New York, 1979.
36. Johnson, W. C. and Cahn, J. W., *Acta metall.*, 1984, **32**, 1925.
37. Lee, J. K., in *Superalloys 1996*, ed. R. D. Kissinger, D. J. Deye, D. L. Anton, A. D. Cetel, M. V. Nathal, T. M. Pollock and D. A. Woodford. The Minerals, Metals and Materials Society, 1996.
38. Laszlo, F., *J. Iron Steel Inst.*, 1945, **2**, 207.
39. Aaronson, H. I., Barnett, D. M., Lee, J. K. and Russell, K. C., *Scr. metall.*, 1974, **8**, 1447.
40. Christensen, R. M., *Mechanics of Composite Materials*, Wiley, New York, 1979.

APPENDIX A

Method of Matched Asymptotic Expansions

We now present a very brief sketch of the matched asymptotic expansion procedure used to obtain the field equations (22)–(24) and boundary conditions of equations (27)–(30). A more detailed derivation may be found in [34].

The idea of the method is to expand the composition c and displacement $\mathbf{u}$ in powers of γ both away from the transition region (the outer expansion) and inside the transition region (the inner expansion). For the outer expansion, i.e. the expansion in the regions Ω^{γ}, we take

$$c(x, y, t) = c^{(0)}(x, y, t) + \gamma c^{(1)}(x, y, t) + \gamma^2 c^{(2)}(x, y, t) + \cdots \quad (43)$$

$$\mathbf{u}(x, y, t) = \mathbf{u}^{(0)}(x, y, t) + \gamma \mathbf{u}^{(1)}(x, y, t) + \gamma^2 \mathbf{u}^{(2)}(x, y, t) + \cdots \quad (44)$$

All the other quantities (e.g. strain, misfit, chemical potential) may be similarly expanded using these fundamental expansions. Plugging the resulting expansions into the DI equations (14) and (15) and equating powers of γ yields (outer) equations valid in $\Omega^{M,P}$.

For the inner expansion, we use a stretched local normal-tangential coordinate system (with respect to Γ). Let $\Gamma = (X(s, t), Y(s, t))$ where s is arclength and t is time. Then, introduce a stretched local coordinate transformation from (x, y) to (z, s) where $z = r/\gamma$ and r is the signed distance along the normal from a point (x, y) to Γ. The orientation of Γ is chosen so that the normal $n = (Y_{,s}, -X_{,s})$ points into the region Ω^{M}. Note that as $\gamma \to 0$, the inner region extends from $-\infty < z < +\infty$. In this coordinate system, the gradient and time derivative operators are

$$\nabla = \frac{1}{\gamma}\hat{n}\frac{\partial}{\partial z} + \left(\frac{1}{1+\gamma z\kappa}\right)\hat{s}\frac{\partial}{\partial s}, \quad \frac{\partial}{\partial t} = -\frac{V}{\gamma}\frac{\partial}{\partial z} + O(\gamma^0), \quad (45)$$

where κ is the mean curvature of Γ and $V = -r_{,t}$ is the normal velocity of Γ. We now change variables and take components of the displacement vector in the normal and tangential directions,

$$c(x, y, t) = \hat{c}(z, s, t), \quad (46)$$

$$\mathbf{u}(x, y, t) = \hat{u}(z, s, t)\hat{n} + \hat{v}(z, s, t)\hat{s}. \quad (47)$$

As in the outer expansion, we expand $\hat{c}$, $\hat{u}$ and $\hat{v}$ in non-negative powers of γ. The inner expansions of all the other fields can be derived from these expansions and the change of variable formulae (equation (45)). Inner equations (valid in the interface layer) are obtained by plugging these expansions into the DI equations (14) and (15) and equating powers of γ.

The solutions of the inner and outer equations are linked across the interface Γ by requiring that as $z \to \pm\infty$, the inner solutions match the outer solutions as $(x, y) \to \Gamma$ from Ω^{M} and Ω^{P}. See [31, 34] for details on this matching procedure. The field equations and boundary conditions claimed in Section 4 follow directly.